

Article

Identification of Industrial Heat Source Production Areas Based on SDGSAT-1 Thermal Infrared Imager

Dacheng Wang ¹, Yanmei Xie ^{1,2}, Caihong Ma ^{1,2,*} , Yindi Zhao ² , Dongmei Yan ^{1,2,3}, Hongyu Chen ⁴, Bihong Fu ⁵, Guangtong Wan ^{1,2} and Xiaolin Hou ^{1,2}

¹ Aerospace Information Research Institute, Chinese Academy of Sciences, Beijing 100094, China; ts22160114p31@cumt.edu.cn (X.H.)

² College of Environment and Spatial Informatics, China University of Mining and Technology, Xuzhou 221116, China

³ University of Chinese Academy of Sciences, Beijing 100049, China

⁴ Institute of Optoelectronics, Fudan University, Shanghai 200433, China

⁵ Innovation Academy for Microsatellites, Chinese Academy of Sciences, Shanghai 201204, China

* Correspondence: mach@aircas.ac.cn; Tel.: +86-152-1067-5780

Abstract: Industrial heat sources (IHSs) are key contributors to anthropogenic heat, air pollution, and carbon emissions. Accurately and automatically detecting their production areas (IHSPAs) on a large scale is vital for environmental monitoring and decision making, yet this is challenged by the lack of high-resolution thermal data. Sustainable Development Science Satellite 1 (SDGSAT-1) thermal infrared spectrometer (TIS) data with the highest resolution (30 m) in the civilian field and a three-band advantage were first introduced to detect IHSPAs. In this study, an IHSPA identification model using multi-features extracted from SDGSAT-1 TIS and Landsat OLI data and support vector machine (SVM) was proposed. First, three brightness temperatures and four thermal radiation indices using SDGSAT-1 TIS and Landsat OLI data were designed to enlarge the temperature difference between IHSPAs and the background. Then, 10 features combined with three indices from Landsat OLI images with the same spatial resolution (30 m) and stable data were extracted. Second, an IHSPA identification model based on SVM and multi-feature extraction was constructed to identify IHSPAs. Finally, the IHS objects were manually delineated and verified using the identified IHSPAs and Google Earth images. Some conclusions were obtained from different comparisons in Wuhai, China: (1) IHSPA identification based on SVM using thermal and optical features can detect IHSPAs and obtain the best results compared with different features and identification models. (2) The importance of using thermal features from the SDGSAT-1 TIS to detect IHSPAs was demonstrated by different importance analysis methods. (3) Our proposed method can detect more IHSs, with greater spatial coverage and smaller areas, compared with the methods of Ma and Liu. This new way to detect IHSPAs can obtain higher-spatial-resolution emissions of IHSs on a large scale and help decision makers target environmental monitoring, management, and decision making in industrial plant processing.

Keywords: industrial heat source production areas; SDGSAT-1 TIS; multi-feature extraction; target identification



Citation: Wang, D.; Xie, Y.; Ma, C.; Zhao, Y.; Yan, D.; Chen, H.; Fu, B.; Wan, G.; Hou, X. Identification of Industrial Heat Source Production Areas Based on SDGSAT-1 Thermal Infrared Imager. *Appl. Sci.* **2024**, *14*, 2450. <https://doi.org/10.3390/app14062450>

Academic Editor: Mario Gai

Received: 6 February 2024

Revised: 27 February 2024

Accepted: 11 March 2024

Published: 14 March 2024



Copyright: © 2024 by the authors. Licensee MDPI, Basel, Switzerland. This article is an open access article distributed under the terms and conditions of the Creative Commons Attribution (CC BY) license (<https://creativecommons.org/licenses/by/4.0/>).

1. Introduction

Industrial heat source production areas (IHSPAs) specifically refer to areas where waste heat is released from working industrial plants, such as from the smelting and rolling of nonferrous metals in oil refineries and exploration fields, cement plants, and chemical processing plants [1]. Industrial heat sources (IHSs) serve as the primary source of production for numerous economic sectors, providing essential material and technical foundations for a country's total energy consumption [2,3]. Heat emissions from IHSs are the main source of anthropocentric heat emissions [4], regional air pollution, and

anthropomorphic carbon emissions [5,6]. In 2022, global carbon dioxide (CO₂) emissions originating from energy combustion and industrial processes experienced a growth of 0.9% and reached a new all-time high of 36.8 gigatons (Gt) according to recent data [7]. Long-term air pollution not only harms human health but also impedes the green and healthy development of nature. What is more, the detection of IHSPAs can also be used to observe the production statuses of factories [8,9]. Therefore, it has become fairly important to detect IHSPAs objectively and accurately to support environmental monitoring and industrial decision making.

Many studies have examined the industrial waste heat potential from the perspectives of energy efficiency and policy [10,11]. Some have concentrated on national- or regional-level heat emissions [12,13] via inventory-based methods, energy balance residuals, the construction of energy models [14], multi-methods [15], and statistical regression methods [13,16,17]. Estimations of waste heat that can be recovered, used again, and utilized by various technologies are one of the key goals of these investigations. However, these methods are limited to exploring the waste heat generated by manufacturing facilities and do not extend to the detection and monitoring of IHSs on a large scale. Moreover, inventory-based methods have difficulty mapping or detecting IHSPAs precisely and objectively from regional to larger scales because of the high subjectivity, time consumption, and data limits [4,17,18].

Recently, high-resolution optical [19] and thermal remote sensing data have been widely utilized to detect and monitor changes in IHSs in large-scale areas [20–22]. Chen et al. [19] identified key equipment by using high-resolution optical images obtained from Worldview and then monitored the illegal and irregular construction of steel firms in Shijiazhuang. However, it is difficult to detect whether firms are working or not, or even to estimate their heat emissions. As a result of its sensitivity to information regarding surface thermal radiation, thermal infrared remote sensing is commonly employed to monitor changes in surface temperatures [20,22–24] using the VIIRS night-fire product (750 m) in conjunction with spatial and temporal features to detect global heat sources. To detect IHSs in small areas by using an adaptive K-means algorithm, VIIRS active fire point data (ACF, 375 m) with a greater spatial resolution were introduced [21]. Later, Ma used VIIRS ACF data to analyze the spatial distribution of heavy IHSs in India based on K-means clustering and threshold identification models combined with nighttime lighting data [25]. The results showed that this detection technique is superior to the “clustering-threshold” technique in terms of accuracy. Lai extracted heat source objects from 2013 data with an accuracy of 97.30% by using VIIRS ACF data combined with DBSCAN clustering and logistic regression clustering algorithms [26]. However, such methods can detect only the approximate locations of IHSs. It is difficult to detect IHSPAs and IHSs lower than 500 K and smaller than $1 \times 10^5 \text{ m}^2$ [27]. Zhou [22] and Zhang [24] used the Landsat 8/9 thermal infrared sensor (TIRS) to construct thermal anomaly indices, such as the heat island intensity index and the heat island radiation index, to distinguish much smaller IHSs. However, it is still challenging to identify IHSPAs precisely.

Sustainable Development Science Satellite 1 (SDGSAT-1) launched on 5 November 2021, and its thermal infrared sensor (TIS) with a 30 m spatial resolution is a significant addition of data for Earth observation because of its highest spatial resolution in the civilian field and three-band advantage [28]. It has been widely used for target detection and monitoring, such as ship detection [29,30], sea surface temperature retrieval, monitoring near nuclear power plants [31], and arctic sea ice lead monitoring [32]. Therefore, nighttime SDGSAT-1 TIS data were first introduced to identify IHSPAs and improve the recognition accuracy and granularity of IHSs. To distinguish IHSPAs from the background, SDGSAT-1 TIS and Landsat 8 OLI data were used to extract multi-features that combine temperature features and optical features. Then, an IHSPA identification model using the multi-features extracted from SDGSAT-1 TIS and Landsat OLI data and support vector machine (SVM) was proposed. First, three brightness temperatures and four thermal radiation indices using SDGSAT-1 TIS and Landsat OLI data were designed to enlarge the temperature difference

between the IHSPAs and the background in IHS areas. Then, 10 features combined with three indices from Landsat OLS images with the same spatial resolution (30 m) and stable data were extracted. Second, an IHSPA identification model based on SVM and multi-feature extraction was constructed to identify IHSPAs. Our results showed that our new model can detect IHSPAs and obtain much smaller IHSs. Finally, the IHS objects were manually delineated and verified using the identified IHSPAs and Google Earth images. This new way to detect IHSPAs can obtain higher-spatial-resolution emissions of IHSs on a large scale and help decision makers target environmental monitoring, management, and decision making in industrial plant processing.

The study area, data sources, and methods are all described in Section 2. The results of the identification utilizing various feature combinations and approaches are examined and discussed in Section 3. The results identified in this paper and the existing IHS data are compared, the study's limitations are discussed, and prospects for future work are outlined in Section 4. Finally, a summary is given in Section 5.

2. Materials and Methods

2.1. Study Area

The study area has a total area of 27,754 km² and includes the cities of Ordos, Yinchuan, Wuhai, and other nearby areas (as illustrated in Figure 1). The region's latitude spans from 37°54' N to 39°35' N, and its longitude is between 105°39' and 108°04' E. It is located at the intersection of the Ningxia Hui Autonomous Region and the Inner Mongolia Autonomous Region. It is a typical industrial heat source area because of the abundance of coal, ores, and nonferrous metal resources [33].

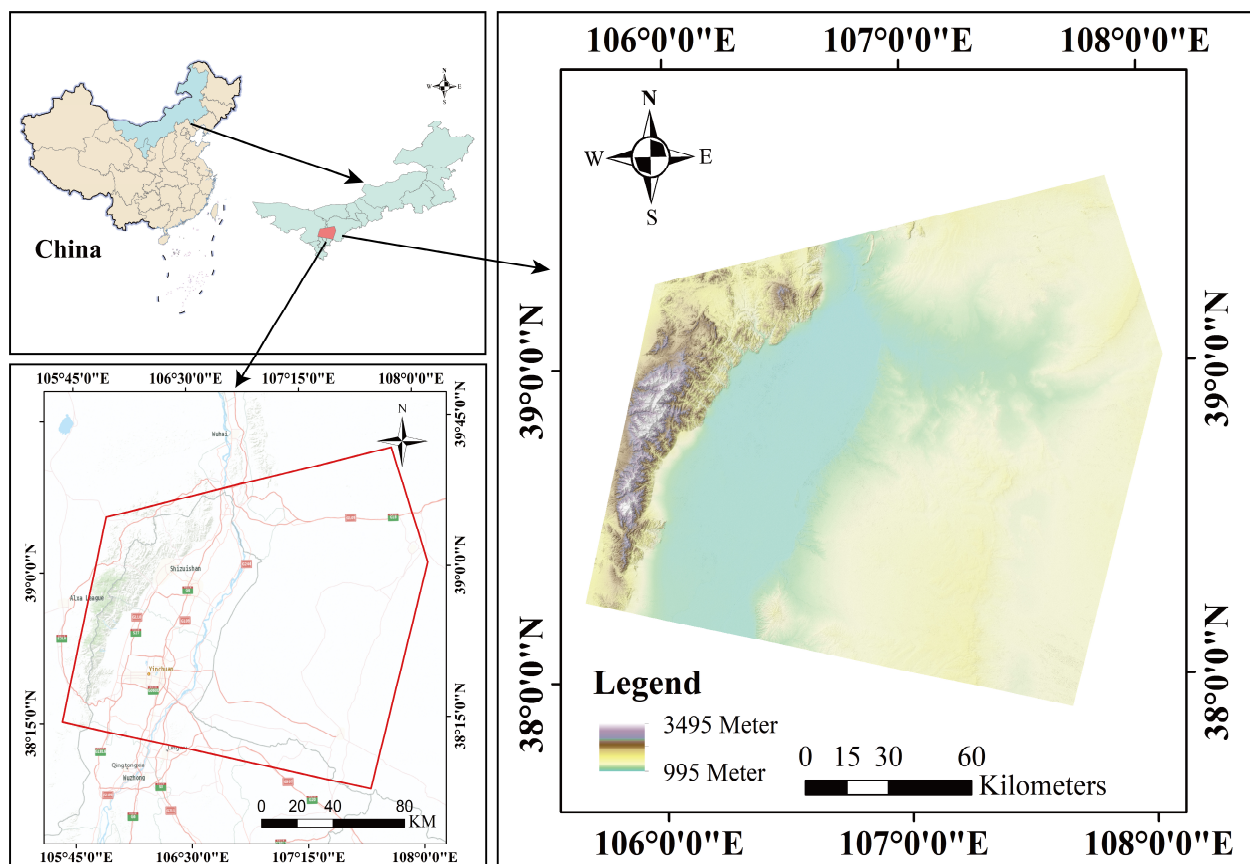


Figure 1. Study area. The study area is 27,754 km², including the cities of Ordos, Yinchuan, Wuhai, and other nearby areas (marked red masks) in North China. It is a typical industrial heat source area because of the abundance of coal, ores, and nonferrous metal resources.

2.2. Data Sources

2.2.1. Sustainable Development Goal Satellite 1 Thermal Infrared Imager Product

SDGSAT-1 was successfully launched as the world's first space science satellite in support of the Sustainable Development Goals (SDGs) on 5 November 2021 [28]. The satellite carries a 30 m resolution TIS, a 10 m resolution multi-spectral imager (MII), and a 10/40 m resolution microlight image (GIU) [34]. It has an imaging width of 300 km and a temporal resolution of 11 days. The TIS image has 3 thermal infrared bands, namely, Band 1 (8.0~10.5 μm), Band 2 (10.60~11.19 μm), and Band 3 (10.50~12.51 μm). Three thermal bands provide a substantial advantage over two thermal bands in that the three-channel split-window technique allows for more precision in land surface temperature retrieval and environmental monitoring [34]. The TIS, combined with MII and GIU data from SDGSAT-1, can provide valuable information that can be utilized to depict human activities and urbanization. The data can be utilized to support both the "Belt and Road Initiative" and programs promoting sustainable development [35].

SDGSAT-1 flies in a sun-synchronous orbit at a 505 km altitude and an inclination angle of 97.5°. It can gather several types of datasets through its synergistic observations both during the day and at night by operating in the "TIS + MII", "TIS + GI", and single-payload observing modes in orbit. Therefore, TIS images contain data from the day and night. The daytime surface thermal radiation mainly contains the reflection of shortwave radiation from the sun and the longwave radiation emitted by the surface object itself, and it is influenced by the type of surface coverage. The night TIS data were adopted to depict the thermal radiation emitted from one object. Therefore, cloudless SDGSAT-1 TIS data on the evening of 15 June 2022 were utilized from <http://124.16.184.48:6008/home> (accessed on 27 August 2022).

2.2.2. Landsat-8 OLI Product

Landsat 8 is the eighth satellite in the U.S. Landsat program, launched successfully on 11 February 2013 from Vandenberg, California. It carries the Operational Land Imager (OLI) with a 30 m resolution and a TIS with 100 m [36]. With a radiometric resolution of 12 bits and a temporal resolution of 16 days, each Landsat-8 scene covers an extensive area of 185 \times 185 km² [37]. Landsat-8 data can be applied across a range of scientific research fields, such as agriculture, urban planning, and environmental monitoring, to provide crucial Earth observation data. Currently, only Collection-2 data are available for distribution. The Collection-1 product stopped production on 31 December 2022, and the Collection-2 product started production on 1 January 2022 [38]. Now, only Landsat Collection-2 products will be produced. While Level-2 data can be utilized directly for quantitative studies, Level-1 data require radiometric calibration for other research purposes, as they are only geometrically rectified.

Landsat-8 OLI data, with the same spatial resolution as the SDGSAT-1 TIS data and stable data quality, were used to extract the optical features of IHSPAs. Therefore, Landsat-8 Collection-2 Level-2 data on 16 June 2022 were chosen from the United States Geological Survey (USGS) website (<https://www.usgs.gov>, accessed on 26 August 2022) in this study.

2.2.3. Auxiliary Data

For spatial calculation and analysis, the World Geodetic System (WGS) 1984 UTM Zone 48° N coordinate system was used. High-resolution (0.5 m) remote sensing data acquired from Google Earth were used to validate the reliability of the IHS products. To verify the validity of our results, Ma's inventory based on active fire point data [21] and Liu's inventory based on night-fire data [3] of IHSs were used. Table 1 displays the details of the datasets used in this study.

Table 1. The information on the data used in this paper. The CBAS refers to the International Research Center of Big Data for Sustainable Development Goals.

Dataset Name		Producer	Period	Resolution	Website
SDGSAT-1 TIS product		CBAS	15 June 2022	30 m	http://124.16.184.48:6008 (accessed on 27 August 2022)
Landsat-8 OLI product		USGS and NASA	16 June 2022	30 m	https://www.usgs.gov (accessed on 26 August 2022)
High-resolution optical images		DigitalGlobe, EarthSat, etc.	/	0.5 m	Google Earth (https://www.google.cn , (accessed on 22 August 2022))
IHS datasets	Liu's datasets	Liu's team	2018	Polygon	https://doi.org/10.1016/j.rse.2017.10.019 (accessed on 9 October 2022)
	Ma's datasets	Ma's team	2018	Polygon	https://doi.org/10.3390/su10124419 (accessed on 7 September 2022)
Administrative divisions		National Centre for Basic Geographic Information	2020	Polygon	https://www.webmap.cn (accessed on 18 September 2022)

2.3. Method

To distinguish IHSPAs from the background, SDGSAT-1 TIS data with the highest resolution (30 m) in the civilian field and a three-band advantage were first introduced to detect IHSPAs. Then, an IHSPA identification model using SDGSAT-1 TIS and the combination of multi-feature extraction and SVM was proposed in this study. It mainly contains four parts: data preprocessing, multi-feature extraction, the IHSPA identification model based on SVM, and IHSPA identification/validation (as shown in Figure 2).

2.3.1. Data Preprocessing

Radiometric calibration is a critical step in remote sensing data processing that involves converting raw radiation values received by sensors into precise and comparable measures of the surface reflectance or radiant brightness [39]. This transformation is essential for ensuring data accuracy and consistency across different acquisitions [40]. Because the unprocessed SDGSAT-1 TIS data contain only digital numbers (DNs), radiometric calibration is needed. In this paper, post-launch calibration based on parameters taken from the data file was used to transform the SDGSAT-1 TIS data. The spectral radiance was calculated by the following formula:

$$L_i = DN_i \times GAIN_i + BIAS_i \quad (1)$$

where DN_i is the pixel value of the i th band, and i (set in {1,2,3}), as shown in Table 1, represents the band identification number of the SDGSAT-1 TIS. $GAIN_i$ and $BIAS_i$ are the calibration gain and offset values, respectively. They can be obtained from the corresponding "*.calib.xml" file. In this context, the values of the radiation calibration parameters can be seen in Table 2. L_i is the spectral radiance value.

Table 2. Values of radiation calibration parameters on SDGSAT-1 TIS. The spectral radiance value of each TIS band can be calculated by the GAIN and BIAS values based on Equation (1).

Band (Band Center (μm))	GAIN	BIAS
Band 1 (9.35)	0.003784	0.163435
Band 2 (10.73)	0.003901	0.125908
Band 3 (11.72)	0.005159	0.205793

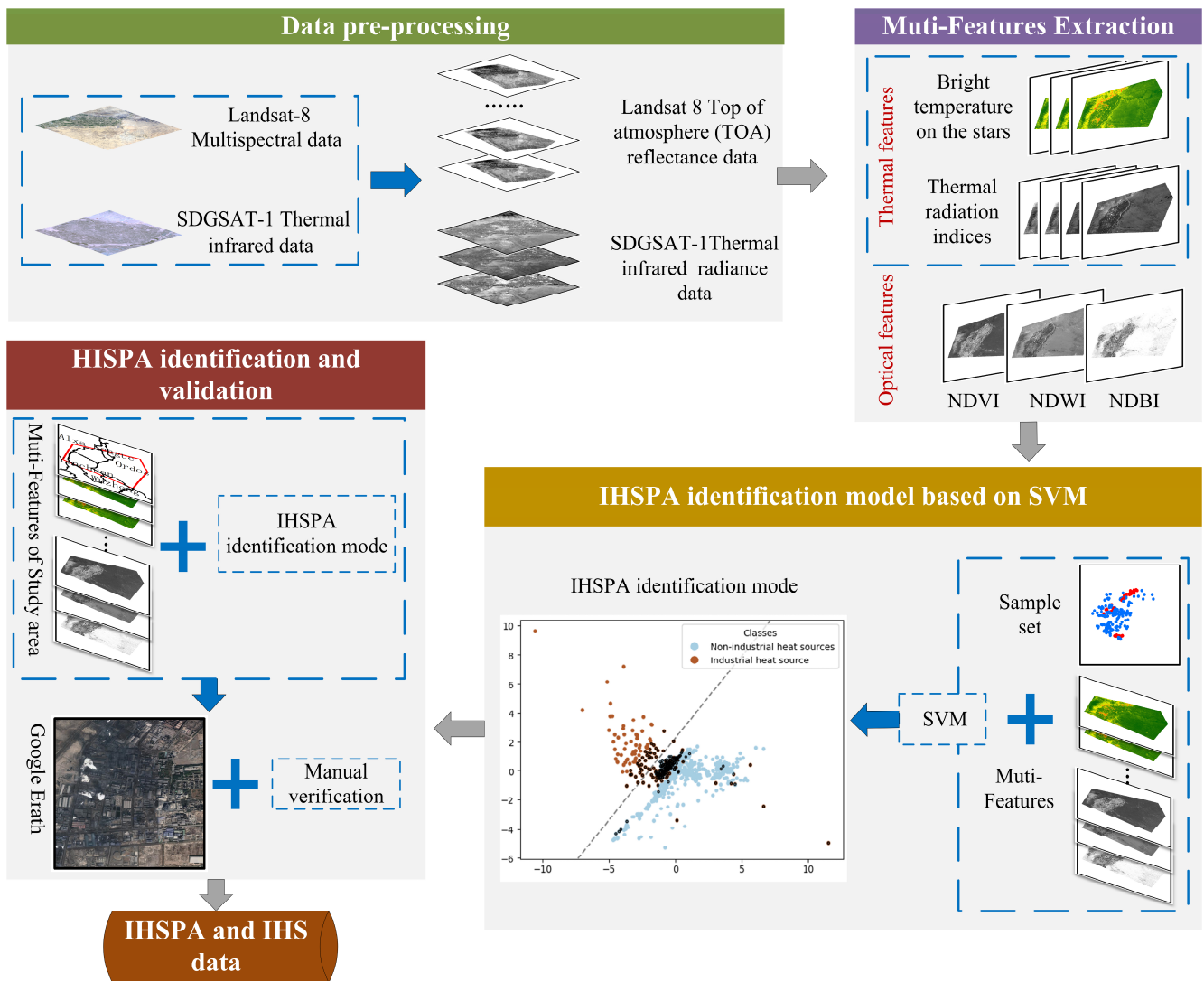


Figure 2. Flow chart of the IHSPA identification model using the SDGSAT-1 TIS and the combination of multi-feature extraction and SVM. It can be divided into four parts: (1) Radiometric calibration of SDGSAT-1 TIS and Landsat-8 data was performed in data preprocessing. (2) Four thermal radiation indices based on three brightness temperatures of SDGSAT-1 TIS data were designed to enlarge the temperature difference between the IHSPAs and background in IHS areas. Then, 10 multi-features, which combined thermal features and optical features, were produced and extracted using SDGSAT-1 TIS and Landsat-8 data. (3) An IHSPA identification model based on SVM with a “small sample advantage” was designed to identify IHSPAs. (4) IHSPAs were detected and validated based on the detection model constructed in part 3.

Landsat-8 Level-2 products are generated by applying additional corrections to Level-1 products to remove spatially, temporally, and especially variable atmospheric effects. In the absence of atmospheric scattering or absorption effects, the Level-2 data provide estimates of the target surface reflectance as determined in situ [41]. To obtain the actual value of Landsat-8 Collection-2 Level-2 data, the reflectance data need to be multiplied by a scaling factor of 0.0000275 and added to a constant of -0.2 [42].

2.3.2. Multi-Feature Extraction

Temperature features that consider heat emissions are the most evident characteristics for detecting IHSPAs. However, it is difficult to clearly distinguish IHSPAs from non-IHSs based on only temperature features, especially on water and road land covers. Optical

features, including color, texture, and spectral features that use the visible and near-infrared spectral range properties of an object or region, can distinguish industrial plants from other land covers [43]. Therefore, thermal features and optical features (as shown in Table 3) were combined to identify IHSPAs precisely.

Table 3. The description of multi-features based on thermal features and optical features. Ten features were obtained by our method from SDGSAT-1 TIS and Landsat-8 OLI data. They include 3 brightness temperature features T_1 , T_2 , and T_3 , 4 thermal radiation index features (RI_1 , RI_2 , RI_3 and RI_4), and 3 optical features (NDVI, NDBI, and NDWI).

Number	Feature Type	Name	Notes	Original data
1	Thermal features	T_1	Satellite brightness temperature of Band 1	SDGSAT-1 TIS data
2		T_2	Satellite brightness temperature of Band 2	SDGSAT-1 TIS data
3		T_3	Satellite brightness temperature of Band 3	SDGSAT-1 TIS data
4		RI_1	Thermal radiation indices $RI_1 = \frac{T_2 - T_1}{T_2 + T_1}$	SDGSAT-1 TIS data
5		RI_2	Thermal radiation indices $RI_2 = \frac{T_3 - T_1}{T_3 + T_1}$	SDGSAT-1 TIS data
6		RI_3	Thermal radiation indices $RI_3 = \frac{T_2 - T_1}{\rho_{NIR}}$	SDGSAT-1 TIS data and Landsat-8 OLI data
7		RI_4	Thermal radiation indices $RI_4 = \frac{T_3 - T_1}{\rho_{NIR}}$	SDGSAT-1 TIS data and Landsat-8 OLI data
8	Optical features	NDVI	Normalized difference vegetation index $NDVI = \frac{\rho_{NIR} - \rho_R}{\rho_{NIR} + \rho_R}$	Landsat-8 OLI data
9		NDBI	Normalized difference built-up index $NDBI = \frac{\rho_{SWIR} - \rho_{NIR}}{\rho_{SWIR} + \rho_{NIR}}$	Landsat-8 OLI data
10		NDWI	Normalized difference water index $NDWI = \frac{\rho_G - \rho_{NIR}}{\rho_G + \rho_{NIR}}$	Landsat-8 OLI data

Notes: ρ_{NIR} is the reflection value in the NIR band, ρ_R is the reflection value in the red band, ρ_{SWIR} is the reflection value in the mid-wave IR, and ρ_G is the reflection value in the green band.

(1) Thermal features

Thermal features include satellite brightness temperatures and thermal radiation indices of the SDGSAT-1 TIS. Satellite brightness temperatures contain three radiation brightness temperatures of each band of the SDGSAT-1 TIS. They can be calculated by Planck’s Law as shown in Formula (2):

$$T_i = \frac{hc}{\lambda_i \times k \times \ln\left(1 + \frac{2hc^2}{\lambda_i \times u^5}\right)} \tag{2}$$

where T_i is the satellite brightness temperature of Band i of the SDGSAT-1 TIS in Kelvin. k is the Boltzmann’s constant (1.38×10^{-23} J/S). h is the Planck’s constant (6.626×10^{-34} J.S). c is the velocity constant of light in a vacuum (2.998×10^8 m/s). λ_i represents the central wavelength of the emitted radiation band (i) (μm).

To describe the temperature difference between IHSPAs and the background, four thermal radiation indices that use brightness temperature values of two different bands of the SDGSAT-1 TIS were designed. They can be calculated by the following formulas:

$$RI_1 = \frac{T_2 - T_1}{T_2 + T_1} \tag{3}$$

$$RI_2 = \frac{T_3 - T_1}{T_3 + T_1} \tag{4}$$

$$RI_3 = \frac{T_2 - T_1}{\rho_{NIR}} \tag{5}$$

$$RI_4 = \frac{T_3 - T_1}{\rho_{NIR}} \quad (6)$$

where T_1 , T_2 , and T_3 are the satellite brightness temperatures of SDGSAT-1 TIS Band 1, Band 2, and Band 3. ρ_{NIR} represents the reflectance value on the near-infrared band of the Landsat-8 OIL data.

(2) Optical features

Optical features are extracted from optical remote sensing images by sensors that detect electromagnetic radiation in the visible, near-infrared, and sometimes shortwave infrared regions of the electromagnetic spectrum [44]. They provide valuable information about the Earth's surface, especially land cover information [45]. They are essential in various remote sensing applications, including land cover classification, vegetation health monitoring, and the detection of land use and land cover changes [46–48]. The normalized difference vegetation index (NDVI) [49], building index (NDBI) [18], and water index (NDWI) [50] are three important and widely applied optical feature indices used to analyze and monitor different aspects of the Earth's surface. Therefore, the above three indices were introduced to distinguish IHSPAs from other land covers in this study.

Considering the absence of the medium infrared band of the SDGSAT-1-MII data, which is essential to extract the NDBI, Landsat-8 OLI data with stable data quality and the same spatial resolution as the SDGSAT-1 TIS data were used to extract the NDVI, NDBI, and NDWI. These optical indices were calculated from Landsat-8 OLI data by using the corresponding spectral bands [51].

The data preprocessing and multi-feature extraction processes in this study, including calculations of the radiance, brightness temperature, thermal radiation indices, and optical indices, were implemented using code written in Python.

2.3.3. Industrial Heat Source Production Area Identification Model Based on SVM

Due to SVM's "small sample advantage" [52], it was introduced to construct an IHSPA identification model. First, sample points (IHSPA samples and non-IHSPA samples) based on Google Earth images and SDGSAT-1 satellite brightness temperature data were constructed. The IHSPA samples were labeled as positive, indicating areas within factory boundaries exhibiting significantly higher thermal radiation anomalies. Non-IHSPA samples, marked as negative, refer to locations that might resemble factory structures but do not show elevated thermal radiation anomalies or areas with high thermal radiation and that, upon inspection via Google Earth imagery, are not factories, potentially misleading the model identification. Then, the multi-features described in Section 2.3.2 of the sample points were extracted.

Second, an IHSPA identification model based on SVM was constructed using sample data. This stage was divided into the following steps. Initially, samples characterized by multi-features were input, followed by their random division into training and testing samples at a ratio of 8:2, with both sets maintained strictly independent from one another. Test sample points were used to assess the reliability and quality of the IHSPA identification model. Subsequently, the built-in SVM model on MATLAB was employed for training. The adjustment of the RBF kernel's cost and gamma parameters was necessary when utilizing SVM. The GridSearch method, widely applied and suitable for optimizing multiple parameters simultaneously, was utilized in this study. The tuning of the cost and gamma was facilitated by setting step sizes, enabling the systematic optimization of the parameters within specified ranges. The values of the cost were $2^{\text{cost}_{\min}}$, $2^{\text{cost}_{\min} + \text{cstep}}$, \dots , $2^{\text{cost}_{\max}}$, and the values of the gamma were $2^{\text{gamma}_{\min}}$, $2^{\text{cost}_{\min} + \text{gstep}}$, \dots , $2^{\text{gamma}_{\max}}$. In this study, $\text{cstep} = 1$ and $\text{gstep} = 1$ were set as the step values, with cost_{\min} and gamma_{\min} established at -3 , and cost_{\max} and gamma_{\max} established at 8 . The approach ensured the identification of the optimal parameters. Finally, the best parameters and training samples were utilized to train an SVM model for the identification of IHSPAs. Then, IHSPAs in the study area were identified based on the IHSPA identification model. Multi-feature data within the study

area were inputted, and the model output a binary raster map, with 0 indicating an IHSPA and 1 denoting a non-IHSPA.

Finally, the IHS objects were manually delineated and verified using the identified IHSPAs and Google Earth images. Pixels with three consecutive values of 1 were considered as an IHS object, and Google imagery was overlaid as a base map to construct the boundaries of the IHS. The constructed IHS objects were then manually verified to confirm their authenticity as real IHSs.

3. Results

3.1. Comparative Performance of Different Features and Identification Models on IHSPA Detection

In this study, we tested different feature combinations for identifying IHSPAs to demonstrate the effectiveness of combining thermal and optical features. Five tests were conducted using Landsat-8 optical features (LOFs), Landsat-8 temperature features (LTFs), SDGSAT-1 thermal features (S-1TIFs), Landsat-8 optical and temperature features (LOFs & TFs), and Landsat-8 optical and SDGSAT-1 thermal infrared features (LOFs & S-1TIFs) within the unified framework. The Landsat-8 optical features consisted of the NDVI, NDWI, and NDBI. Landsat-8 temperature features were derived from the temperature of Landsat-8 Band 10. The specific combination of features is shown in Table 4.

Table 4. Different combination methods of features. Five combination models were created using SDGSAT-1 TIS data and Landsat-8 OLI data to demonstrate the effectiveness of our multi-features. LOFs (Landsat-8 optical features), LTFs (Landsat-8 temperature features), and S-1TIFs (SDGSAT-1 thermal features) represent the use of only one type of feature (optical features or thermal features) and one remote sensing dataset (SDGSAT-1 TIS data or Landsat-8 OLI data). LOF & TF (Landsat-8 optical and temperature features) combined optical and temperature features and used Landsat-8 OLI data. LOFs & S-1TIFs (Landsat-8 optical features and SDGSAT-1 thermal features) are the multi-features produced in this paper.

Abbreviation	Full Name	Number of Features	Features	Feature Source Data
LOFs	Landsat-8 optical features	3	NDVI, NDBI, NDWI	Landsat-8 OLI data
LTFs	Landsat-8 temperature features	1	$T_{\text{Landsat-8}}$	Landsat-8 OLI data
S-1TIFs	SDGSAT-1 thermal features	7	$T_1, T_2, T_3, RI_1, RI_2, RI_3, RI_4$	SDGSAT-1 TIS data
LOFs & TFs	Landsat-8 optical and temperature features	4	NDVI, NDBI, NDWI, $T_{\text{Landsat-8}}$	Landsat-8 OLI data
LOFs & S-1TIFs	Landsat-8 optical features and SDGSAT-1 thermal features	10	NDVI, NDBI, NDWI, $T_1, T_2, T_3, RI_1, RI_2, RI_3, RI_4$	SDGSAT-1 TIS data and Landsat-8 OLI data

To verify the effectiveness of identifying IHSPAs based on SVM, three comparison machine learning classifiers, decision tree (DT) [53], k-nearest neighbor (KNN) [54], and naive Bayes (NB) [55], were selected in this study. These accuracies were obtained for each classifier under the conditions of the corresponding attributes of the samples, optimal classifier parameters, and ten times tenfold cross-validation.

Table 5 and Figure 3 show the accuracy and visual results obtained from different features and identification models for IHSPA detection. According to the results in Table 5, LOFs & S-1TIFs had the highest identification accuracy compared to the other features. SDGSAT-1 thermal infrared features (S-1TIFs) also achieved high accuracy compared with the LOFs, LOFs & TFs, and LTFs. LOFs & S-1TIFs and S-1TIFs can distinguish IHSPAs from the background much more clearly (as shown in Figure 3). Additionally, four classifiers were assessed, and the IHSPA identification based on SVM produced the most accurate

results in all four classifiers. In summary, the IHSPA identification based on SVM using thermal and optical features from SDGSAT-1 thermal infrared data and Landsat-8 data obtained the best IHSPA results.

Table 5. Comparison of different features and identification models for IHSPA detection: accuracy. Five feature combination models and four detection methods were compared to verify the effectiveness of identifying IHSPAs based on multi-features and SVM in this paper.

Experiment	Classifier			
	DT	KNN	NB	SVM
LOFs	86.94%	89.63%	75.79%	90.05%
LTFs	81.05%	81.99%	81.08%	83.51%
S-1TIFs	89.83%	89.42%	89.29%	91.24%
LOFs & TFs	89.07%	81.71%	77.35%	90.66%
LOFs & S-1TIFs	90.87%	90.41%	91.74%	92.39%

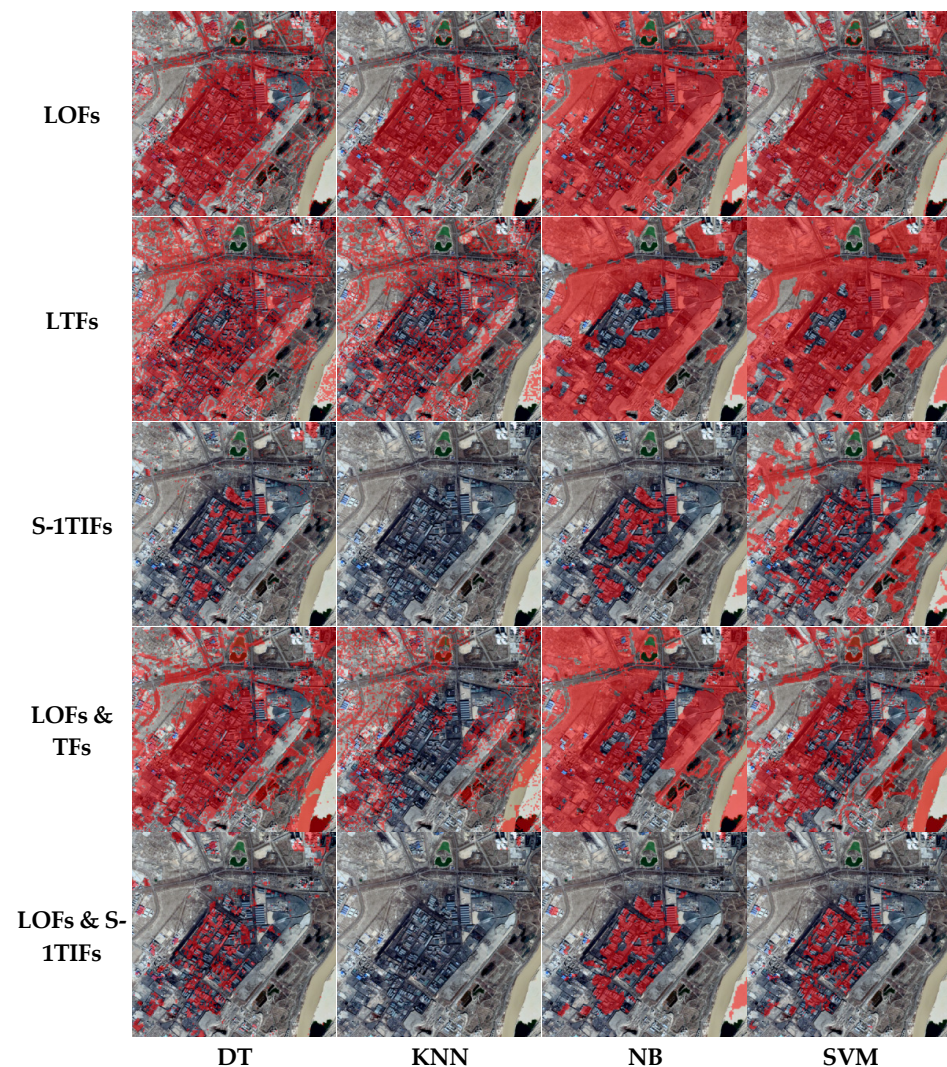


Figure 3. Visualization of identified IHSPAs (marked red masks) using different features and classifiers. IHSPAs combined with S-1TIFs or LOFs & S-1TIFs and DT or NB and SVM can be distinguished more accurately. Some buildings in residential areas based on S-1TIFs or LOFs & S-1TIFs and DT areas were easily misidentified as IHSPAs. Some sandy shores based on S-1TIFs or LOFs & S-1TIFs and NB areas were also easily misidentified. Only IHSPA detection results combined with LOFs & S-1TIFs and SVM obtained the best results.

3.2. Importance Analysis of Different Features to Identify IHSPAs

To estimate the relative importance weights of different features in identifying IHSPAs, the built-in functions of the SVM and neighborhood component analysis (NCA) [56] were used. First, the importance weights of the feature factors of the radial kernel function (RBF) SVM model were ranked using SVM built-in functions. The weights were listed in order from highest to lowest: NDBI, T₁, NDWI, T₃, NDVI, T₂, RI₂, RI₃, RI₄, and RI₁.

NCA is supervised learning based on stochastic KNN, which uses the leave-one-out method to measure the similarity of nearest neighbors with the help of metric learning and cross-validation. It can effectively use objective optimization to reduce the conditionality of the input data and can be used to calculate the feature weights. The importance results based on NCA are listed in Table 6. They show that T₁ had the largest weight, followed by the NDBI, RI₂, RI₃, NDWI and T₂. The importance of thermal features in model training was demonstrated by both evaluation methodologies.

Table 6. Feature importance weights based on NCA. NCA methods were used to evaluate the importance weights of 10 different features to identify IHSPAs. The importance results were ranked in descending order of weight values. Higher weight values indicate greater importance.

Feature	T1	NDBI	RI2	RI3	NDWI	T2	NDVI	T3	RI4	RI1
Weight	2.22	2.09	2.00	1.61	1.51	1.16	0.89	0.27	0.43	0.14

4. Discussion

4.1. Comparison with Existing IHS Data

To generate industrial heat source objects from IHSPAs, a manual industrial heat source object identification method using high-resolution remote sensing images was adopted. Then, SDGSAT-1 TIS and the combination of multi-feature extraction and SVM were used to identify 371 IHS objects from the IHSPA results. The 339 objects were verified as real IHSs via multiple manual validations that used Google Earth images (0.5 m). The identification accuracy was 91.37% (339/371).

To compare and analyze the effectiveness of our new model, our results were compared with Ma's inventory based on active fire point data [21] and Liu's inventory based on night fires [3]. A total of 66 and 44 IHSs were obtained from Ma (2018) and Liu (2018), respectively. In addition, 65 (98.48%) and 43 (97.73%) objects, respectively, were verified as real IHSs via multiple manual validations. Although the recognition accuracy of our results was lower than those of the Ma and Liu inventories, our results identified many more industrial heat source objects. Our method is the only method that can detect IHSPAs precisely.

The average area, minimum area, maximum area, and total area of industrial heat source objects were statistically analyzed from our results and Ma's and Liu's inventories. The final statistical results are shown in Table 7. Figure 4 shows the spatial distributions of our results and those of Ma's and Liu's inventories. From Table 7 and Figure 4, some conclusions can be obtained:

- (1) The number of our results was 5.22 times greater than the number of Ma's inventory and 7.88 times greater than that of Liu's inventory. This suggests that our method, due to improvements in the thermal infrared data resolution and sensitivity to low-temperature objects, may identify a greater number of factories with smaller scales and lower levels of thermal radiation;
- (2) The total area of IHSs identified by our study was 666.89 km², which was 332.08% and 286.99% more than the areas identified by Ma and Liu (200.82 km²/232.37 km²), respectively. At the same time, the minimum identification area of our results was 0.03 km², rather than the 0.16 km² and 0.26 km² of Ma's and Liu's inventories, respectively. This means that the IHSs based on our method were granular with greater precision. It improved the phenomenon of "one industrial heat source object covering multiple factories and mines";

- (3) The spatial coverages of our results for Ma’s and Liu’s inventories were 93.85% (61/65) and 79.55% (35/44), respectively, which were higher than the spatial coverages of Ma’s and Liu’s inventories for our results (74.67% and 62.14%, respectively).

Table 7. Comparison of our results with Ma’s and Liu’s inventories. A total of 371 IHSs were identified from the IHSPA results by a manual identification method using high-resolution remote sensing images. A total of 371 IHS objects were compared with Ma’s inventory based on active fire point data [21] and Liu’s inventory based on night fires [3]. The accuracy and some area information of the IHSs were calculated.

	True	False	Total Number	Accuracy	Average Area (km ²)	Minimum Area (km ²)	Maximum Area (km ²)	Total Area (km ²)
Our result	339	32	371	91.37%	1.80	0.03	68.95	666.89
Ma’s data	65	1	66	98.48%	3.04	0.16	52.52	200.82
Liu’s data	43	1	44	97.73%	5.28	0.26	28.37	232.37

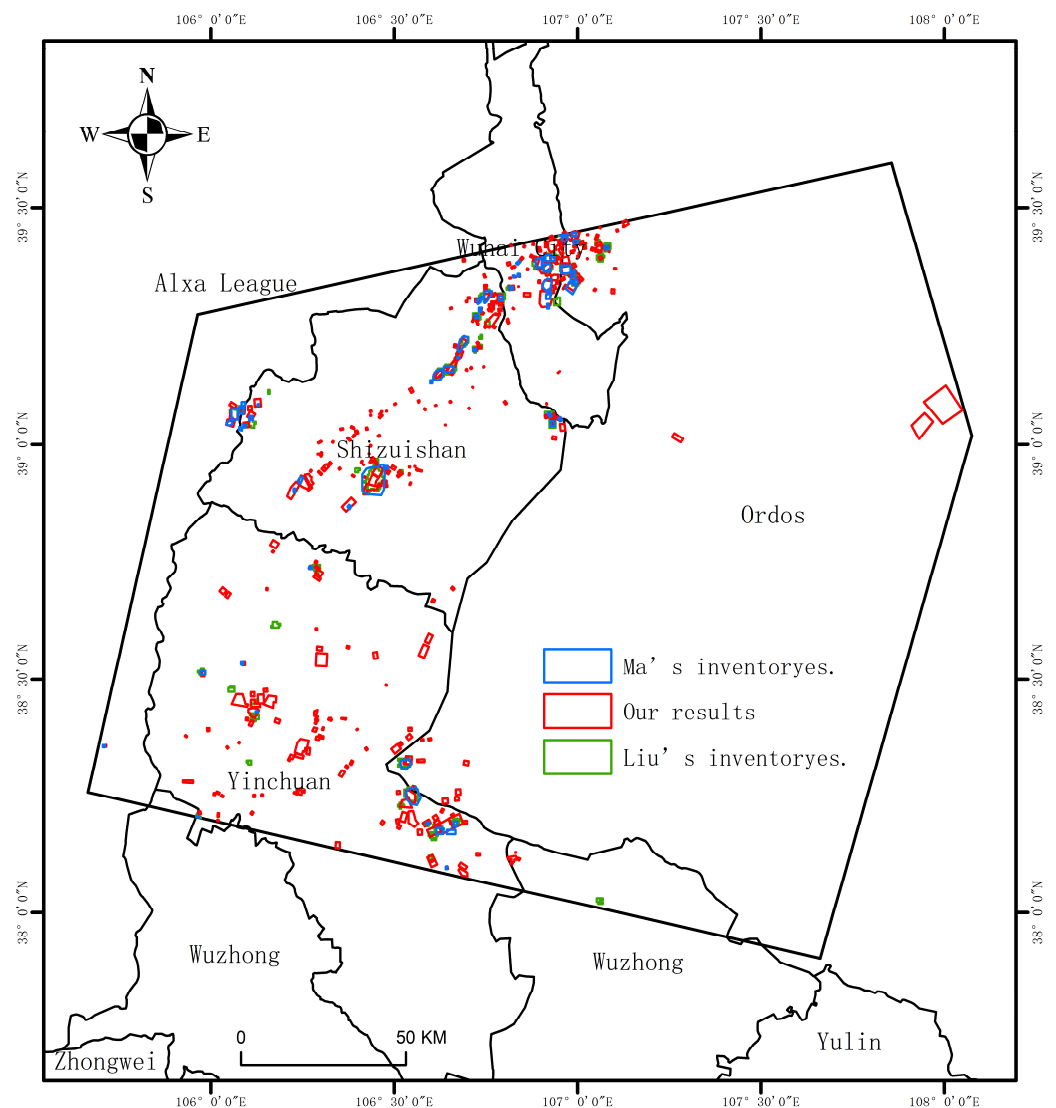


Figure 4. Comparison of our results with IHSs detected by Liu et al. [3] and Ma et al. [21]. The blue, green, and red polygon-labeled areas represent IHS objects detected by Ma, Liu, and our results, respectively. There are many more of our IHS objects (red polygons) and they cover a broader spatial layout, while the IHS objects in the other two datasets have high spatial overlap.

4.2. Limitations and Prospects for Future Work

In this research, SDGSAT-1 TIS data with the highest resolution (30 m) in the civilian field and a three-band advantage were first introduced to detect IHSPAs. Our results on the study area estimated that the proposed method can improve the granularity and accuracy of IHS detection. To ensure the consistency of IHSPA products, new features based on land surface temperature (LST) data of the SDGSAT-1 TIS will be constructed to detect IHSPAs easily and depict the difference between different IHSs clearly. Additionally, a new automatically constructed IHS model using IHSPAs will be built and used in this study, as opposed to the manual method.

It is worth noting that SDGSAT-1 TIS data, especially nighttime TIS data, are inevitably impacted by cloud contamination. Future studies should also focus on removing clouds from nighttime SDGSAT-1 TIS data or on finding more cloudless SDGSAT-1 TIS data to detect IHSPAs on a large scale in different seasons with complex topography using SDGSAT-1 TIS and Landsat-8 OLI data. We also intend to research the connection between IHSPAs or IHSs and economic development and to keep working to determine more about the relationship between climate change and carbon neutrality. These are also important issues in the Paris Agreement [57,58].

5. Conclusions

Large-scale heat and pollution emissions from IHSs can have serious impacts on environmental quality and human health and cause climate change and natural disasters. However, the existing methods are unable to accurately identify IHSPAs, and the granularity of the IHS identification is low. Therefore, SDGSAT-1 TIS data, which have the highest resolution (30 m) in the civilian field and a three-band advantage, were first introduced to detect IHSPAs and improve the granularity and accuracy of IHS detection. Then, an IHSPA identification model using SDGSAT-1 (TIS) and the combination of multi-feature extraction and SVM was proposed in this research. Some conclusions were obtained from different comparisons in Wuhai, China:

- (1) IHSPA identification based on SVM using thermal and optical features from SDGSAT-1 TIS and Landsat-8 data can detect IHSPAs and obtain the best IHSPA results compared with different features and identification models;
- (2) The importance of thermal features in model training was demonstrated by different importance analysis methods. T_1 from the SDGSAT-1 TIS had the largest importance weight;
- (3) Our proposed method can detect more IHSs with greater spatial coverage and smaller areas than the methods of Ma [21] and Liu [3]. The number of IHSs from our results was 5.22 times greater than the number from Ma's inventory and 7.88 times greater than the number from Liu's inventory. At the same time, the minimum identification area of our results was 0.03 km², rather than the 0.16 km² and 0.26 km² of Ma's and Liu's inventories, respectively.

The results suggest that our method, due to improvements in the thermal infrared data resolution and sensitivity to low-temperature objects, may identify a greater number of factories with smaller scales and lower levels of thermal radiation. And industrial plants and mines can be monitored and evaluated more precisely by utilizing our IHSPA identification model employing SDGSAT-1 TIS data. This method could be useful to industry regulations and policymakers.

Author Contributions: Conceptualization, D.W., Y.X., C.M., Y.Z. and D.Y.; methodology, Y.X., C.M., Y.Z. and D.Y.; software, Y.X. and C.M.; validation, D.W. and Y.X.; formal analysis, Y.X. and C.M.; investigation, Y.X., C.M., Y.Z., D.Y., X.H., H.C., B.F. and G.W.; resources, C.M.; data curation, Y.X., C.M., Y.Z., D.Y., X.H., H.C., B.F. and G.W.; writing—original draft preparation, Y.X., C.M. and Y.Z.; writing—review and editing, D.W., Y.X., C.M., and Y.Z.; visualization, Y.X. and C.M.; supervision, C.M., Y.Z. and D.Y.; project administration, D.W., C.M., Y.Z. and D.Y.; funding acquisition, D.W. and C.M. All authors have read and agreed to the published version of the manuscript.

Funding: This research was supported by the National Key R&D Program of China (No. 2022YFF0606402) and the Youth Innovation Promotion Association of the Chinese Academy of Science under Grant 2021126.

Institutional Review Board Statement: Not applicable.

Informed Consent Statement: Not applicable.

Data Availability Statement: The authors acknowledge the free use of Landsat-8 OLI products (<https://earthexplorer.usgs.gov/>, accessed on 26 August 2022). The SDGSAT-1 TIS data were kindly provided by the International Research Center of Big Data for Sustainable Development Goals (CBAS).

Acknowledgments: The authors thank the editors and the three anonymous reviewers for their valuable comments, which helped to improve our manuscript.

Conflicts of Interest: The authors declare no conflicts of interest.

References

- Inayat, A. Current progress of process integration for waste heat recovery in steel and iron industries. *Fuel* **2023**, *338*, 127237. [CrossRef]
- Ma, C.; Yang, J.; Xia, W.; Liu, J.; Zhang, Y.; Sui, X. A Model for Expressing Industrial Information Based on Object-Oriented Industrial Heat Sources Detected Using Multi-Source Thermal Anomaly Data in China. *Remote Sens.* **2022**, *14*, 835. [CrossRef]
- Liu, Y.; Hu, C.; Zhan, W.; Sun, C.; Murch, B.; Ma, L. Identifying Industrial Heat Sources Using Time-Series of the VIIRS Nightfire Product with an Object-Oriented Approach. *Remote Sens. Environ.* **2018**, *204*, 347–365. [CrossRef]
- Chen, Q.; Yang, X.; Ouyang, Z.; Zhao, N.; Jiang, Q.; Ye, T.; Qi, J.; Yue, W. Estimation of anthropogenic heat emissions in China using Cubist with points-of-interest and multisource remote sensing data. *Environ. Pollut.* **2020**, *266*, 115183. [CrossRef]
- Park, C.; Jeong, S.; Park, H.; Yun, J.; Liu, J. Evaluation of the Potential Use of Satellite-Derived XCO₂ in Detecting CO₂ Enhancement in Megacities with Limited Ground Observations: A Case Study in Seoul Using Orbiting Carbon Observatory-2. *Asia-Pac. J. Atmos. Sci.* **2020**, *57*, 289–299. [CrossRef]
- Shi, X.; Xu, Y. Evaluation of China's Pilot Low-Carbon City Program: A Perspective of Industrial Carbon Emission Efficiency. *Atmos. Pollut. Res.* **2022**, *13*, 101446. [CrossRef]
- IEA. *CO₂ Emissions in 2022—Analysis*; IEA: Paris, France, 2023. Available online: <https://www.iea.org/reports/co2-emissions-in-2022> (accessed on 2 May 2023).
- Han, F.; Zhao, F.; Li, F.; Shi, X.; Wei, Q.; Li, W.; Wang, W. Improvement of Monitoring Production Status of Iron and Steel Factories Based on Thermal Infrared Remote Sensing. *Sustainability* **2023**, *15*, 8575. [CrossRef]
- Zhao, H.; Ma, Y.; Chen, F.; Liu, J.; Jiang, L.; Yao, W.; Yang, J. Monitoring Quarry Area with Landsat Long Time-Series for Socioeconomic Study. *Remote Sens.* **2018**, *10*, 517. [CrossRef]
- Kosmadakis, G. Estimating the potential of industrial (high-temperature) heat pumps for exploiting waste heat in EU industries. *Appl. Therm. Eng.* **2019**, *156*, 287–298. [CrossRef]
- Moser, S.; Jauschnik, G. Using Industrial Waste Heat in District Heating: Insights on Effective Project Initiation and Business Models. *Sustainability* **2023**, *15*, 10559. [CrossRef]
- Hong, G.-B.; Pan, T.-C.; Chan, D.Y.-L.; Liu, I.-H. Bottom-up analysis of industrial waste heat potential in Taiwan. *Energy* **2020**, *198*, 117393. [CrossRef]
- Koralegedara, S.B.; Lin, C.-Y.; Sheng, Y.-F.; Kuo, C.-H. Estimation of anthropogenic heat emissions in urban Taiwan and their spatial patterns. *Environ. Pollut.* **2016**, *215*, 84–95. [CrossRef]
- Sailor, D.J. A review of methods for estimating anthropogenic heat and moisture emissions in the urban environment. *Int. J. Climatol.* **2011**, *31*, 189–199. [CrossRef]
- Chow, W.T.; Salamanca, F.; Georgescu, M.; Mahalov, A.; Milne, J.M.; Ruddell, B.L. A multi-method and multi-scale approach for estimating city-wide anthropogenic heat fluxes. *Atmos. Environ.* **2014**, *99*, 64–76. [CrossRef]
- Lee, S. Sensitive detection of NMR for thin films. *Solid State Nucl. Magn. Reson.* **2015**, *71*, 1–10. [CrossRef] [PubMed]
- Lee, S.-H.; McKeen, S.A.; Sailor, D.J. A regression approach for estimation of anthropogenic heat flux based on a bottom-up air pollutant emission database. *Atmos. Environ.* **2014**, *95*, 629–633. [CrossRef]
- Guha, S.; Govil, H.; Gill, N.; Dey, A. A long-term seasonal analysis on the relationship between LST and NDBI using Landsat data. *Quat. Int.* **2020**, *575–576*, 249–258. [CrossRef]
- Chen, P.; Lu, L.; Zhu, H.; Zhu, Y.; Wang, Y. Research on the Suitability of Image at Different Resolutions for the Identification of Steel Enterprise Using Remote Sensing. *J. Geo-Inf. Sci.* **2015**, *17*, 1119–1127. [CrossRef]
- Lai, J.; Zhu, J.; Chai, J.; Xu, B. Spatial-Temporal Analysis of Industrial Heat and Productivity in China. *Appl. Geogr.* **2022**, *138*, 102618. [CrossRef]
- Ma, C.; Yang, J.; Chen, F.; Ma, Y.; Liu, J.; Li, X.; Duan, J.; Guo, R. Assessing Heavy Industrial Heat Source Distribution in China Using Real-Time VIIRS Active Fire/Hotspot Data. *Sustainability* **2018**, *10*, 4419. [CrossRef]
- Zhou, Y.; Zhao, F.; Wang, S.; Liu, W.; Wang, L. A Method for Monitoring Iron and Steel Factory Economic Activity Based on Satellites. *Sustainability* **2018**, *10*, 1935. [CrossRef]

23. Shivers, S.W.; Roberts, D.A.; McFadden, J.P. Using paired thermal and hyperspectral aerial imagery to quantify land surface temperature variability and assess crop stress within California orchards. *Remote Sens. Environ.* **2019**, *222*, 215–231. [[CrossRef](#)]
24. Zhang, Z.; He, G.; Peng, Y.; Long, T.; Wang, M.; Wei, M. Landsat surface temperature products over China. *China Sci. Data* **2020**, *5*, 74–82. [[CrossRef](#)]
25. Ma, C.; Niu, Z.; Ma, Y.; Chen, F.; Yang, J.; Liu, J. Assessing the Distribution of Heavy Industrial Heat Sources in India between 2012 and 2018. *ISPRS Int. J. Geo-Inf.* **2019**, *8*, 568. [[CrossRef](#)]
26. Lai, J. *Study on Remote Sensing Identification Andspatial Distribution Pattern of Heat Source in Heavyindustry*; Northwest Normal University: Lanzhou, China, 2020. [[CrossRef](#)]
27. Li, B.; Fan, J.; Han, L.; Sun, G.; Zhang, D.; Zhang, P. An Industrial Heat Source Extraction Method: BP Neural Network Using Temperature Feature Template. *J. Geo-Inf. Sci.* **2022**, *24*, 533–545.
28. Chen, J.; Cheng, B.; Zhang, X.; Long, T.; Chen, B.; Wang, G.; Zhang, D. A TIR-Visible Automatic Registration and Geometric Correction Method for SDGSAT-1 Thermal Infrared Image Based on Modified RIFT. *Remote Sens.* **2022**, *14*, 1393. [[CrossRef](#)]
29. Li, L.; Jiang, L.; Zhang, J.; Wang, S.; Chen, F. A Complete YOLO-Based Ship Detection Method for Thermal Infrared Remote Sensing Images under Complex Backgrounds. *Remote Sens.* **2022**, *14*, 1534. [[CrossRef](#)]
30. Li, L.; Yu, J.; Chen, F. TISD: A Three Bands Thermal Infrared Dataset for All Day Ship Detection in Spaceborne Imagery. *Remote Sens.* **2022**, *14*, 5297. [[CrossRef](#)]
31. Huang, W.; Jiao, J.; Zhao, L.; Hu, Z.; Peng, X.; Yang, L.; Li, X.; Chen, F. Thermal Discharge Temperature Retrieval and Monitoring of NPPs Based on SDGSAT-1 Images. *Remote Sens.* **2023**, *15*, 2298. [[CrossRef](#)]
32. Qiu, Y.; Li, X.-M.; Guo, H. Spaceborne Thermal Infrared Observations of Arctic Sea Ice Leads at 30 m Resolution. *Cryosphere* **2023**, *17*, 2829–2849. [[CrossRef](#)]
33. Song, M.; Hao, X.; Zhang, L.; Song, M.; Cheng, J.; Li, D.; Zhang, W.; Wu, J. Transformation Performance and Subsystem Coupling of Resource-Based Cities in China: An Analysis Based on the Support-Pressure Framework. *Integr. Environ. Assess. Manag.* **2021**, *18*, 770–783. [[CrossRef](#)]
34. Hu, Z.; Zhu, M.; Wang, Q.; Su, X.; Chen, F. SDGSAT-1 TIS Prelaunch Radiometric Calibration and Performance. *Remote Sens.* **2022**, *14*, 4543. [[CrossRef](#)]
35. Rajendran, S.; Al-Kuwari, H.A.-S.; Sadooni, F.N.; Nasir, S.; Govil, H. Remote Sensing of Inland Sabkha and a Study of the Salinity and Temporal Stability for Sustainable Development: A Case Study from the West Coast of Qatar. *Sci. Total Environ.* **2021**, *782*, 146932. [[CrossRef](#)]
36. Chaves, M.E.D.; Picoli, M.C.A.; Sanches, I.D. Recent Applications of Landsat 8/OLI and Sentinel-2/MSI for Land Use and Land Cover Mapping: A Systematic Review. *Remote Sens.* **2020**, *12*, 3062. [[CrossRef](#)]
37. European Space Agency. Sentinel-2—Resolution and Swath—Sentinel Handbook—Sentinel Online. 2020. Available online: <https://sentinel.esa.int/web/sentinel/missions/sentinel-2/instrument-payload/resolution-and-swath> (accessed on 18 December 2022).
38. USGS. *Landsat Collection 2 (Ver. 1.1, January 15, 2021): U.S. Geological Survey Fact Sheet 2021–3002*; U.S. Geological Survey: Menlo Park, CA, USA, 2021. [[CrossRef](#)]
39. Kelcey, J.; Lucieer, A. Sensor correction and radiometric calibration of a 6-band multispectral imaging sensor for UAV remote sensing. *ISPRS-Int. Arch. Photogramm. Remote Sens. Spat. Inf. Sci.* **2012**, *39*, 393–398. [[CrossRef](#)]
40. Tan, K.; Niu, C.; Jia, X.; Ou, D.; Chen, Y.; Lei, S. Complete and accurate data correction for seamless mosaicking of airborne hyperspectral images: A case study at a mining site in Inner Mongolia, China. *ISPRS J. Photogramm. Remote Sens.* **2020**, *165*, 1–15. [[CrossRef](#)]
41. Pinto, C.T.; Jing, X.; Leigh, L. Evaluation Analysis of Landsat Level-1 and Level-2 Data Products Using In Situ Measurements. *Remote Sens.* **2020**, *12*, 2597. [[CrossRef](#)]
42. Wu, T.; Xu, Z.; Chen, R.; Wang, S.; Li, T. Channel Activity Remote Sensing Retrieval Model: A Case Study of the Lower Yellow River. *Remote Sens.* **2023**, *15*, 3636. [[CrossRef](#)]
43. Kang, Y.; Chen, Z.; Li, L.; Zhang, Q. Construction of multidimensional features to identify tea plantations using multisource remote sensing data: A case study of Hangzhou city, China. *Ecol. Inform.* **2023**, *77*, 102185. [[CrossRef](#)]
44. Adjovu, G.E.; Stephen, H.; James, D.; Ahmad, S. Measurement of Total Dissolved Solids and Total Suspended Solids in Water Systems: A Review of the Issues, Conventional, and Remote Sensing Techniques. *Remote Sens.* **2023**, *15*, 3534. [[CrossRef](#)]
45. Gourgiotis, A.; Kyvelou, S.S.; Lainas, I. Industrial Location in Greece: Fostering Green Transition and Synergies between Industrial and Spatial Planning Policies. *Land* **2021**, *10*, 271. [[CrossRef](#)]
46. Hu, B.; Xu, Y.; Huang, X.; Cheng, Q.; Ding, Q.; Bai, L.; Li, Y. Improving Urban Land Cover Classification with Combined Use of Sentinel-2 and Sentinel-1 Imagery. *ISPRS Int. J. Geo-Inf.* **2021**, *10*, 533. [[CrossRef](#)]
47. Hernández-Clemente, R.; Hornero, A.; Mottus, M.; Penuelas, J.; González-Dugo, V.; Jiménez, J.C.; Suárez, L.; Alonso, L.; Zarco-Tejada, P.J. Early Diagnosis of Vegetation Health From High-Resolution Hyperspectral and Thermal Imagery: Lessons Learned From Empirical Relationships and Radiative Transfer Modelling. *Curr. For. Rep.* **2019**, *5*, 169–183. [[CrossRef](#)]
48. Mishra, P.K.; Rai, A.; Rai, S.C. Land use and land cover change detection using geospatial techniques in the Sikkim Himalaya, India. *Egypt. J. Remote Sens. Space Sci.* **2019**, *23*, 133–143. [[CrossRef](#)]
49. Huang, S.; Tang, L.; Hupy, J.P.; Wang, Y.; Shao, G.F. A commentary review on the use of normalized difference vegetation index (NDVI) in the era of popular remote sensing. *J. For. Res.* **2021**, *32*, 2719. [[CrossRef](#)]

50. Teng, J.; Xia, S.; Liu, Y.; Yu, X.; Duan, H.; Xiao, H.; Zhao, C. Assessing habitat suitability for wintering geese by using Normalized Difference Water Index (NDWI) in a large floodplain wetland, China. *Ecol. Indic.* **2020**, *122*, 107260. [[CrossRef](#)]
51. Hussain, S.; Mubeen, M.; Ahmad, A.; Majeed, H.; Qaisrani, S.A.; Hammad, H.M.; Amjad, M.; Ahmad, I.; Fahad, S.; Ahmad, N.; et al. Assessment of Land Use/Land Cover Changes and Its Effect on Land Surface Temperature Using Remote Sensing Techniques in Southern Punjab, Pakistan. *Environ. Sci. Pollut. Res.* **2022**, *30*, 99202–99218. [[CrossRef](#)]
52. Shang, Y.; Zheng, X.; Li, J.; Liu, D.; Wang, P. A Comparative Analysis of Swarm Intelligence and Evolutionary Algorithms for Feature Selection in SVM-Based Hyperspectral Image Classification. *Remote Sens.* **2022**, *14*, 3019. [[CrossRef](#)]
53. Mohebbanaaz; Kumari, L.V.R.; Sai, Y.P. Classification of ECG Beats Using Optimized Decision Tree and Adaptive Boosted Optimized Decision Tree. *Signal Image Video Process.* **2021**, *16*, 695–703. [[CrossRef](#)]
54. Zhang, X.; Xiao, H.; Gao, R.; Zhang, H.; Wang, Y. K-Nearest Neighbors Rule Combining Prototype Selection and Local Feature Weighting for Classification. *Knowl.-Based Syst.* **2022**, *243*, 108451. [[CrossRef](#)]
55. Vu, D.-H. Privacy-Preserving Naive Bayes Classification in Semi-Fully Distributed Data Model. *Comput. Secur.* **2022**, *115*, 102630. [[CrossRef](#)]
56. Diker, A. An Efficient Model of Residual Based Convolutional Neural Network with Bayesian Optimization for the Classification of Malarial Cell Images. *Comput. Biol. Med.* **2022**, *148*, 105635. [[CrossRef](#)] [[PubMed](#)]
57. Oda, T.; Maksyutov, S.; Andres, R.J. The Open-Source Data Inventory for Anthropogenic CO₂, version 2016 (ODIAC2016): A Global Monthly Fossil Fuel CO₂ Gridded Emissions Data Product for Tracer Transport Simulations and Surface Flux Inversions. *Earth Syst. Sci. Data* **2018**, *10*, 87–107. [[CrossRef](#)] [[PubMed](#)]
58. Paris Agreement. Wikipedia. 2023. Available online: https://en.wikipedia.org/w/index.php?title=Paris_Agreement&oldid=1152110861 (accessed on 9 May 2023).

Disclaimer/Publisher’s Note: The statements, opinions and data contained in all publications are solely those of the individual author(s) and contributor(s) and not of MDPI and/or the editor(s). MDPI and/or the editor(s) disclaim responsibility for any injury to people or property resulting from any ideas, methods, instructions or products referred to in the content.